

GNEISS:

GEOPHYSICAL NON-EQUILIBRIUM IONOSPHERIC SYSTEM SCIENCE

Heliophysics Low Cost Access to Space 2022

PI: KRISTINA A LYNCH, Dartmouth

*CoIs: JOHN BONNELL UCB - MEGHAN BURLEIGH NRL - ROB CLAYTON ERAU -
DONALD HAMPTON UAF/GI - LESLIE LAMARCHE SRI - MARC LESSARD UNH -
ROMINA NIKOUKAR APL - MARILIA SAMARA GSFC - MATTHEW ZETTERGREN ERAU*

TABLE OF CONTENTS

NASA Cover Page and Summary

Proposal Document:

Table of Contents	1 page
1 Science	pg 1
1.1 Proposal Goals and Relevance to NASA Goals	pg 1
1.2 Mission Science Questions and Objectives	pg 3
2 Technical	pg 6
2.1 Mission Design and Traceability	pg 6
2.2 Instruments, groundbased	pg 8
2.3 Instruments, in situ	pg 11
2.4 Instruments, lattice	pg 15
2.5 Modelling tools	pg 19
3 Science Closure, Relevance, and Impact for Heliophysics	pg 20
4 Management	pg 20
4.1 Team and Responsibilities	pg 20
4.2 Schedule and work plan	pg 20
References	pg 21
Inclusion Plan	pg 26
DMP: Data management plan	pg 27
CVs, Work Effort, and Support:	
Vitae, Table of personnel and work effort	12 pages
Current and Pending Support	22 pages
Budget and Budget Narrative	34 pages
Facilities and Equipment	1 page

PRD: Proposal Requirements Document

Dartmouth Budgets Document:

Dartmouth College Institutional Budget Justifications
CoI Subcontract Budgets and Justifications
Total project cost to NASA

1 Science

1.1 Proposal Goals and Relevance to NASA Goals

From MICA to Isinglass to GNEISS: “*Gneiss is distinctive among other rocks that have bands because its minerals are not evenly distributed so the bands are various widths.*” –pronounced like “nice”. [Grammarist, 2023]

The GNEISS (Geophysical Non-Equilibrium Ionospheric System Science) mission grows from our group’s nightside auroral rocket studies, starting with the AMICIST [Hallinan *et al.*, 2001], SIERRA [Lynch *et al.*, 2007; Klatt *et al.*, 2005], and MICA [Lynch *et al.*, 2015; Zettergren *et al.*, 2014] mission distinctions between DC and ELF activity. The Cascades2 mission used multiple payloads and imagery to explore connections between visible and in situ signatures. Most recently, the Isinglass mission [Clayton *et al.*, 2019, 2021] emphasized system science enabled by heterogeneous multipoint observational platforms and interpreted through the data-driven GEMINI ionospheric model [Zettergren *et al.*, 2014]

The Isinglass study exploited the along-arc symmetry that is a defining feature of many nightside aurora; however, arcs that vary lengthwise are also quite common and geophysically significant. Folds, bends, and filaments have beautiful structure (often in the 1-50 km range of spatial scales) indicative of the changing state of the ionosphere and its coupling to the magnetosphere. The proposed mission (GNEISS) will further advance our ability to “read” the ionospheric electric and magnetic field information encoded in these structured visible signatures. Figure 1 illustrates how similar, and how different, arcs can be over the 15 sec, 2-degree separation of SWARM-A and SWARM-C crossings of THEMIS-GBO imagery [Themis, 2023; Swarm, 2023]. These examples are drawn from an ongoing database

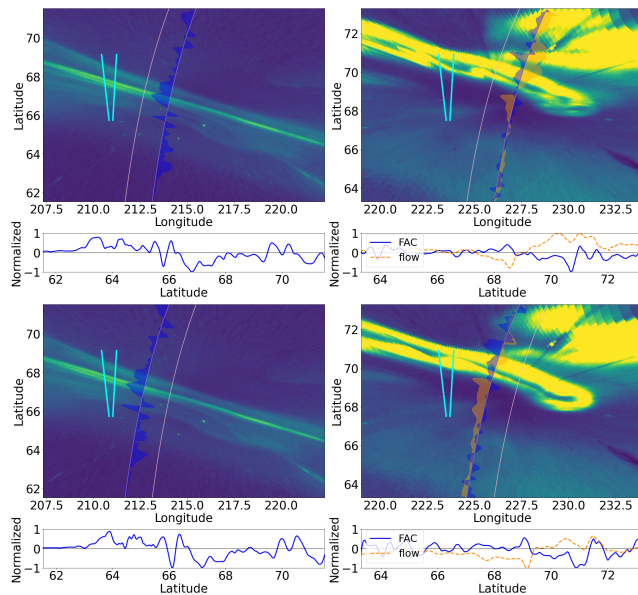


Figure 1: ESA-Swarm in situ conjunctions with Themis-GBO ground images: (left) a highly sheetlike auroral event; (right) a non-sheetlike event with significant along-arc structure. Line plots: field-aligned current (blue) and (when available) cross-track flow velocity (orange) of the ionospheric plasma. “V” symbol: scale size of the GNEISS footprints. Lower panels: the same two events, 15 s later and 2 degrees westward, from a second spacecraft. Note the along-arc-direction consistency of the FAC signatures in the sheetlike case, and the coherent, but varied differences in the in situ FAC and flow of the non-sheetlike case. [Themis, 2023; Swarm, 2023]

study of \sim 14,000 such satellite-imagery conjunctions (\sim 63 of which involve both SWARM-A and -C). In the two left-panel crossings (a sheetlike structure) the magnetic field data are almost indistinguishable at the two crossings. In the two right-panel crossings (a non-sheetlike structure) auroral intensity variations, corresponding to changes in the structure and magnitude of electron acceleration and parallel potential drops, are seen with varied in situ plasma flows and currents.

Studies of the Isinglass launch event [Clayton *et al.*, 2019, 2021] assumed sheetlike structure: viz. the flow field had minimal variation in the along-arc direction. However, a close look at the processed imagery and model results shows that even in this predominantly sheetlike structure, conductance varied significantly along the arc (cf. Figure 2 energy flux (Q) variations). Current closure paths (red “tubes”) at two locations are also shown in Fig. 2, demonstrating differing morphology at various places along the arc. GNEISS represents a transition from the study of sheetlike auroral arcs to the study of non-idealized, non-sheetlike, nightside, discrete auroral structures and addresses situations where system parameters (potential drop, conductivity, flows) have significant zero-order along-arc variations. Arcs with such along-arc structure represent the *vast majority* of active, intense auroral features, and understanding their electric (flows) and magnetic (currents) field structures is key to understanding the details of Magnetosphere-Ionosphere (MI) system energy and momentum deposition by the aurora. Figures 1 and 2 provide hints to the importance of along-arc structure; GNEISS provides a detailed dataset for model driving and analysis, including both multipoint in situ observations and detailed ionospheric density volume information from a variety of platforms. Unlike our SWARM database, this mission will include multi-wavelength optical imagery with concurrent spatially resolved data (e.g. density and fields).

The goal of GNEISS is to gather a fully instrumented multipoint, multiplatform dataset enabling a case study of the 3D ionospheric volume surrounding a non-sheetlike discrete auroral structure – in the context of lattice tomography, auroral-imaged, and radar-profiled E- and F-regions. The ideal target is a westward surge or pre-midnight, discrete, intense-current auroral structure with distinct zero-order along-arc variation.

GNEISS’s NASA relevance is that the physics of what we learn from reading the aurora is important not only for Earth, but also for planetary auroras such as Jupiter. Technical contributions include development of new measurement modalities for multipoint, heterogenous platforms for system science. GNEISS is well aligned with Helio-

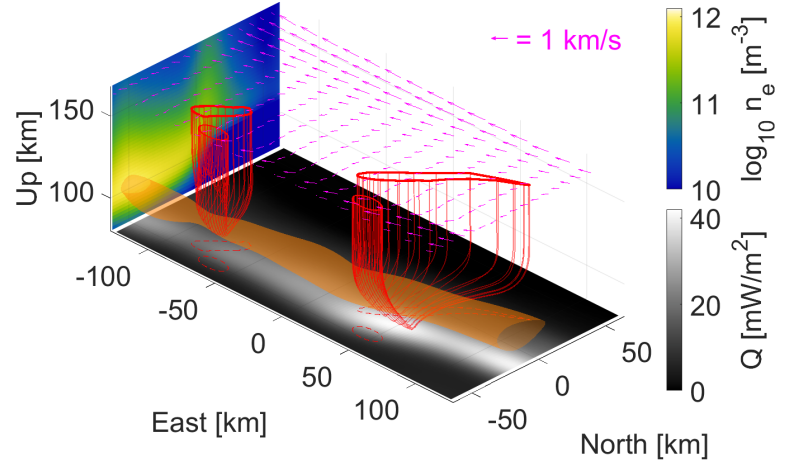


Figure 2: GEMINI 3D model space representation of the Isinglass case study of Clayton *et al.* [2021]. Western panel: a cut of the calculated density volume at the western longitude; orange isosurface: plasma density at $10^{11.9} \text{ m}^{-3}$. Base plane: auroral intensity in grey. Red tubes: current paths. Top vectors: imposed F-region flow field.

physics Goals and Objectives to “Advance our understanding of ... the connections between solar variability and Earth ...” and “Develop the knowledge and capability to detect and predict extreme conditions...” GNEISS is a clear example of the “Diversified and Distributed Sensor Deployment Strategy” envisioned NAS Decadal Appendix C [NRC, 2013].

GNEISS’s distributed measurements, detailed below, are an important first step toward more realistic descriptions and predictive capability for auroral behavior. As a case study it provides needed heterogeneous characterizations of a specific event, while allowing us to develop data processing techniques and instrumentation for more systematic applications to high latitude magnetosphere-ionosphere coupling to be targeted in missions such as GDC (exploring markedly different spatial scales).

1.2 Mission Science Questions and Objectives

1.2.1 Overview

A given instance of F-region plasma flows, volumetric currents, and conductivity volume in the vicinity of an auroral structure must satisfy current continuity throughout the volume [Brekke *et al.*, 1989; Marghitu, 2012]; in height-integrated form this reads:

$$j_z(x, y) = (\nabla \cdot \mathbf{E}) \Sigma_P + \nabla \Sigma_P \cdot \mathbf{E} - \nabla \Sigma_H \cdot (\hat{\mathbf{e}}_1 \times \mathbf{E}) \quad (1)$$

Here $j_z(x, y)$ is the field-aligned current (FAC, positive along \mathbf{B}), \mathbf{E} is the ionospheric electric field, $\hat{\mathbf{e}}_1$ is a unit vector along \mathbf{B} , and Σ_P , Σ_H are the Pedersen and Hall conductances, respectively. This 2D (latitude, longitude) constraint connecting currents, flows, and conductances unfolds into a three-dimensional, time-varying volume - for example as calculated by the GEMINI model in our prior studies with time-dependent drivers (Fig. 2).

For a given ionospheric situation, current continuity provides a known and calculable constraint – provided that parameters of the current continuity equation can be measured/inferred from data. Thus, the system science question at hand is not simply “how does the current close”, as that is defined, e.g., by Eqn. 1. Instead we seek to understand which combinations of space- and time-varying flow, current, and conductivity actually occur in the driven auroral system (i.e. the *parameters* appearing in Eqn. 1), and how they compare with existing electromagnetic models of driven auroral arcs. This information has proven maddeningly difficult to pin down in modeling studies at local, global, and geospace system level scales. Further, we seek to understand how these parameters affect distributions of incoming current, Poynting flux, and plasma in the neighborhood of an auroral arc via spatially-dependent momentum and energy deposition. For idealized sheetlike arcs, many aspects of this behavior are understood and can be predicted [Marghitu, 2012; Robinson *et al.*, 1987; Knight, 1973; Mallinckrodt, 1985]. However, even for a perfectly sheetlike arc, there is along-arc physics (note Fig. 2, and 3(a)), as we will discuss shortly below.

One of the main complexities of the auroral “electric circuit” lies in the co-dependence of electromagnetic field quantities and the thermal and suprathermal plasma state, hence conductivity. The auroral acceleration region (AAR) forms on the basis of field-aligned current carrying requirements dictated by the states of the overlying magnetosphere and underlying ionosphere [Knight, 1973]. At the same time, the AAR and suprathermal particles it generates vastly alter the ionospheric conductivity, perpendicular currents, and, indirectly, parallel current requirements. GNEISS data synthesis and modeling efforts provide a detailed

and data-constrained example of how the 3D MI system places accelerated current carriers, thus changing conductivity patterns, and how the flows and currents evolve around these time-varying drivers. *Such an understanding of the non-local interplay between thermal and suprathermal plasmas in auroras and relation to conserved electromagnetic quantities is a key missing aspect of auroral science and its implications for MI coupling.*

1.2.2 Discussion, examples, modeling case study, targets

The importance of (unappreciated because often-unobserved) along-arc variation can be motivated clearly in a non-height-integrated picture, such as illustrated by the example simulations of Fig. 3. This figure demonstrates results of increasing along-arc structuring with a sequence of ionospheric model (GEMINI) hypothetical simulations. The western slice in each panel of Fig. 3 (with green-yellow colormap) shows a latitude-altitude density slice; the bottom slice (lowest altitude, red/blue colormap) shows the driving topside FAC map, and the tube structures illustrate the GEMINI-calculated current closure patterns. In panel a the driving precipitation and current maps are perfectly sheetlike. Even so, there are along-arc (here east-west) aspects to the closure currents, showing the 3D nature of even an

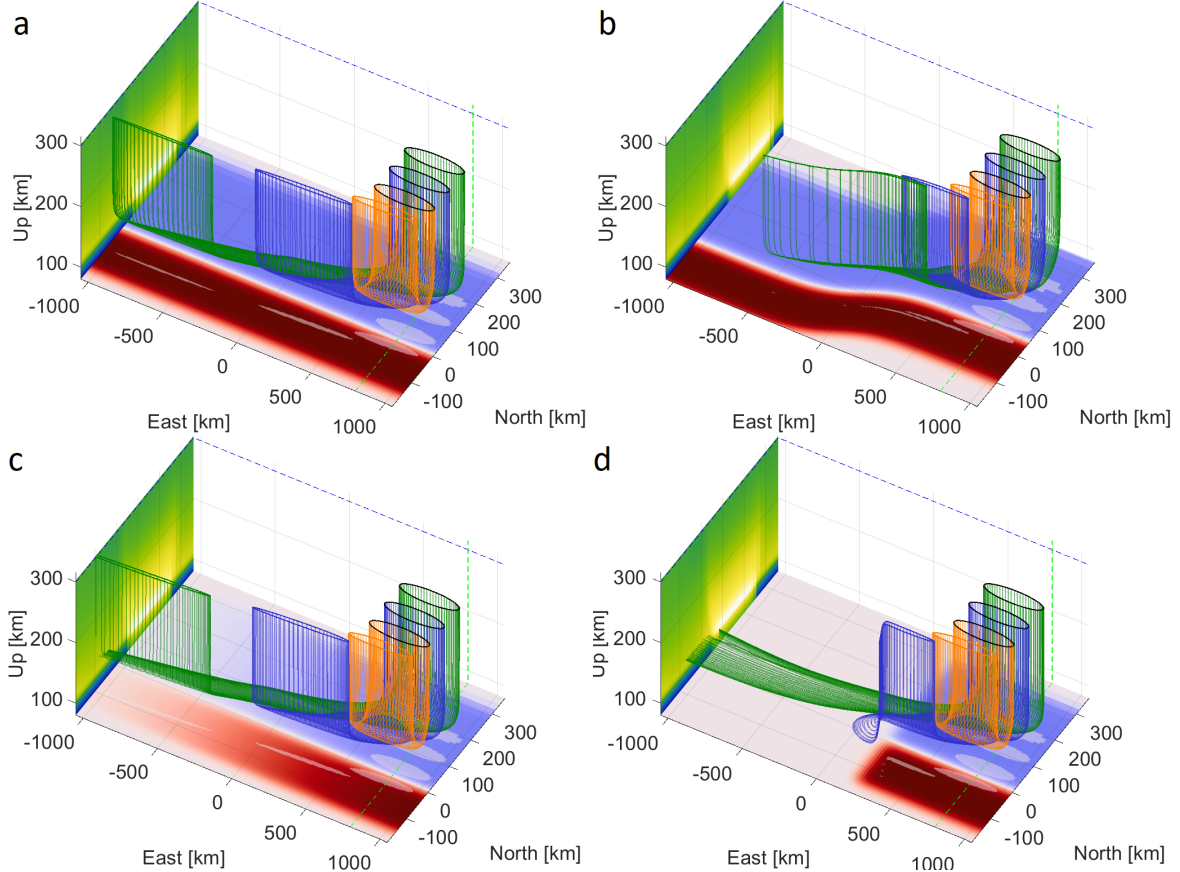


Figure 3: GEMINI model runs. Western panel: plasma density cut at 800 km east ranging from 10^9 to $10^{11.5} \text{ m}^{-3}$. Base panel: imposed FAC cut at 300 km from -2 (blue) to 2 (red) $\mu\text{A}/\text{m}^2$. In each case a 3 keV, 3 mW/m² precipitation map is imposed within the precipitating (blue) FAC region. Tubes: FAC closure structure. (a) null straight FAC structure; (b) bent structure; (c) FAC linearly varying along structure; (d) FAC limited partially across precipitation structure.

apparently sheetlike arc. In panel b a bend is imposed in the simulation drivers, significantly changing the closure patterns. Panel c shows a system where the imposed FAC varies linearly in the direction along the arc. Panel d illustrates a current sheet that terminates abruptly, in the presence of an existing conductance enhancement; here the closure pattern shows a strong funneling into the Hall current. It is notable that all of these patterns are plausible from the standpoint of mimicking patterns found in auroral imagery.

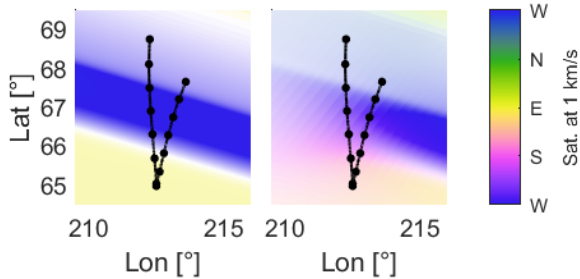


Figure 4: $\mathbf{E} \times \mathbf{B}$ flow maps, in an HSV representation where color indicates direction, from runs (a) and (d) of Fig. 3, but in geographic coordinates. The overlays are ground projections of the GNEISS trajectories.

Figure 4 shows two self-consistent flow map solutions to the same imposed map of precipitation, driven with different maps of imposed FAC (panels a and d of Figure 3) showing markedly different flow fields and demonstrating the need of field observations (and, indeed the full GNEISS experiment) alongside our optical measurements.

The state of knowledge for auroras is such that, via Eqn. 1, we can take maps of either field-aligned current or flow along with a map of precipitation and, with an appropriate model, compute the full system response including remaining electromagnetic quantities like volumetric currents, flows, and $\Delta\mathbf{B}$ and the mass, momentum, and energy response of the plasma. While optical data provide us with mapped estimates of precipitation, there are no measurements of flow or FAC spatial variations for our science targets, i.e. it is not sufficient to measure the electromagnetic fields and particles along one trajectory. One efficient way to obtain such a dataset (albeit for a case study) is simultaneous (or near-simultaneous) rockets launched into an active aurora with ejectable payloads to form multiple in situ measurement baselines (1 km via ejectables and 50 km via main payload separation); and, importantly, to additionally have a distributed volume of measurements of the auroral density throughout the E- and F-region, in order to constrain GEMINI calculations of transport and conductivity. These can be obtained from filtered imagery inversions, radar profiles, and a tomographic lattice of TEC observations. The payload and imagery provide field and particle information while the combined fields-of-view of the ISR and lattice experiments provide slices of plasma density along longitudinally separated planes (Fig. 5). These different platforms provide us with information about variability across the mesoscale feature of the launch event.

In Fig. 4, we illustrate two self-consistent flow map solutions to the same imposed map of precipitation, driven with different maps of imposed FAC (panels a and d of Figure 3) showing markedly different flow fields and demonstrating the need of field observations (and, indeed the full GNEISS experiment) alongside our optical measurements.

What we know: For a given specification (flow map - current map - precipitation map)

we know how the currents will close in the 3D volume, since this is constrained by current continuity in an electrostatic case. For a given conductivity volume, we know what precipitation map corresponds, and vice versa, given model calculations such as *Fang et al.* [2008]; *Robinson et al.* [1987]. And, for a given set of two maps (flow and conductivity, or, FAC and conductivity) we know the third map, as this is what GEMINI can calculate from driving inputs (assuming that GEMINI is the correct model for the situation).

What we do not know: For a given map of the average energy and energy flux of the precipitation, we do not know which current-map/flow-map combinations are valid. How does the system choose between families of possibilities that are consistent with current continuity? As the precipitation map (average energy and energy flux) evolves in time, can we read what that means and infer what that implies about ionospheric currents, flows, and closure patterns? For a given current/flow/image map, can we interpret the drivers and responses? If we can read the aurora, what do we learn? Can we resolve ambiguities such as illustrated below in Fig. 4?

Thus we aim to gather a multipoint, multiplatform dataset in order to study an event such as (a) a “breakup” as in the MICA event just after a surge passage [*Lynch et al.*, 2015]; (b) growth phase arcs and substorm passages as in Isinglass [*Clayton et al.*, 2019, 2021]; (c) a pseudobreakup; or (d) a westward surge with along-arc structure as in Figure 1. GNEISS data will reveal new aspects of auroras (not before measured) which will be used to provide more realistic descriptions of auroral dynamics through processing and synthesis with models.

1.2.3 Science questions

GNEISS addresses science questions related to the 3D nature of the aurora including:

1. What mesoscale latitudinal and, particularly, longitudinal, variations exist in plasma flows (electric fields) and volumetric currents at scales of 1-50km within a non-sheetlike auroral structure’s flow-current-conductivity system?
2. What implications do these non-idealized flow-current-conductivity patterns have for the auroral ionospheric system science (current continuity and energetics) of ionosphere-magnetosphere coupling?

The former question focuses on developing an improved understanding of spatial variation in fields and plasma parameters in a 3D auroral structure (for the first time), while the latter deals with the issue of how these manifest through the full ionospheric volume and affect the exchange of charge and energy through the MI system. Thus, we have both a focus on making new and improved spatially resolved, rocket-borne measurements of the auroral system in the context of distributed density observations, in addition to synthesizing these new measurements through contemporary, local-scale auroral models to develop new understanding of the importance of structured auroral forms.

2 Technical

2.1 Mission Design and Traceability

Figure 5 illustrates the GNEISS mission design, with the left panel illustrating the trajectories, fields of views, and lines of sight; and the right panel illustrating the simulated data fields as interpreted by the GEMINI model. GNEISS consists of **two** near-simultaneously (within a minute) launched, azimuthally near-parallel (10 deg az separation), 300-500 km

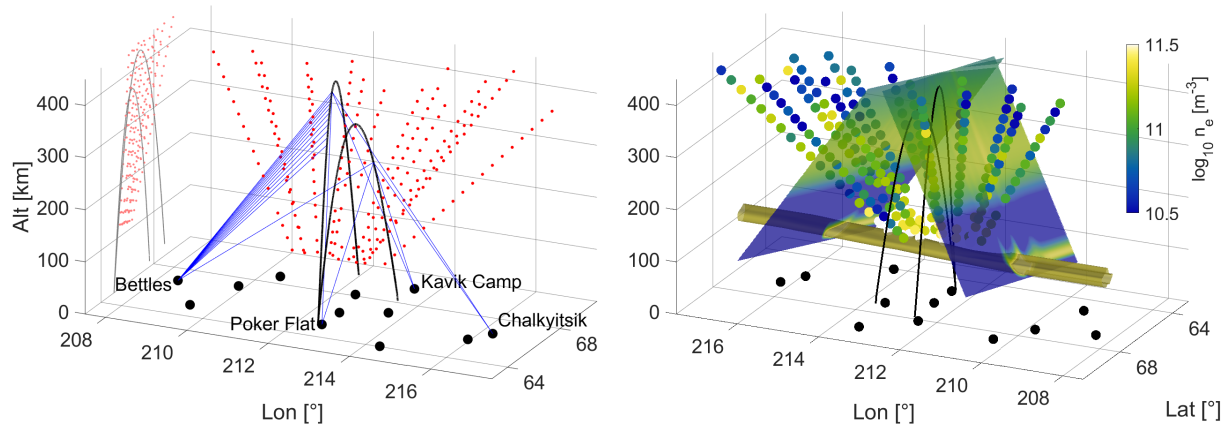


Figure 5: Mission overview diagram. (left) Trajectories (black), lattice and GBO sites (dots), lattice lines-of-sight (blue), and PFISR beams (red), viewed from the south of Poker Flat. (right) View now from the north, with overlays of densities as interpreted by GEMINI and observed by PFISR [Clayton *et al.*, 2021] (density isosurface from Isinglass is $10^{11.4} \text{ m}^{-3}$).

apogee, identically-instrumented **Poker flights** over **multistation filtered auroral imagery groundbased observatories (GBOs)**, connected with a **lattice of line-of-sight tomography rays** between the payloads and up to a dozen VHF **groundbased software radio receivers**, in the context of **nearby PFISR** density volume sensing. The azimuthal separation allows a 50-100 km trajectory separation in the along-arc direction near apogee. Payload hardware includes DC electric field (DCE) and science magnetometer; thermal ions and electrons; requested VHF transmissions for a lattice of Faraday-rotation-TEC sight lines; and deployed “Bob” (thermal ions) and “Rob” (plasma density) subpayloads (spring or rocket propelled) for multipoint thermal plasma proxy observations. Groundbased hardware includes four filtered-imagery GBOs that allow mapping of energy flux and characteristic energy of electron precipitation from auroral emissions; together with 12 small experimenter-supplied software-defined-radio-receivers for the lattice of rays for VHF transmissions from each payload (sensing Faraday rotation for TEC information); and PFISR. The GEMINI physics-based ionospheric model will be used to synthesize these multipoint, multiplatform data into a computational object for use in studying the case event.

2.1.1 Mission design

As illustrated in Fig. 5, the two rocket trajectories provide side-by-side cuts of the same auroral structure. The flat views of Figure 6 show that they are within PFRR Zone 3, using a 10 degree span within the Zone-3 358 deg to 10 deg azimuthal width (as per SRPO guidance, G Marsh.) Recent launches (ACES, Joule II, Trice) have allowed one or two minute separation between launches; a variation in the elevation (apogee) of the two GNEISS flights allows them to reach the same magnetic latitude at the same time, given minute-scale delays between the launches. In the example shown in Figs. 5 and 6(left), the western flight, which needs to reach farther north to cross the magnetic-latitude-aligned arc structure, launches approximately one minute earlier and a little higher than the eastern flight such that both cross the apogee magnetic latitude within a few sec of each other. In an alternate possibility, shown in the right panel of Fig. 6, now with the eastern flight launching one minute earlier, both trajectories reach the same altitude, allowing greater conjunction range but poorer magnetic-latitude alignment.

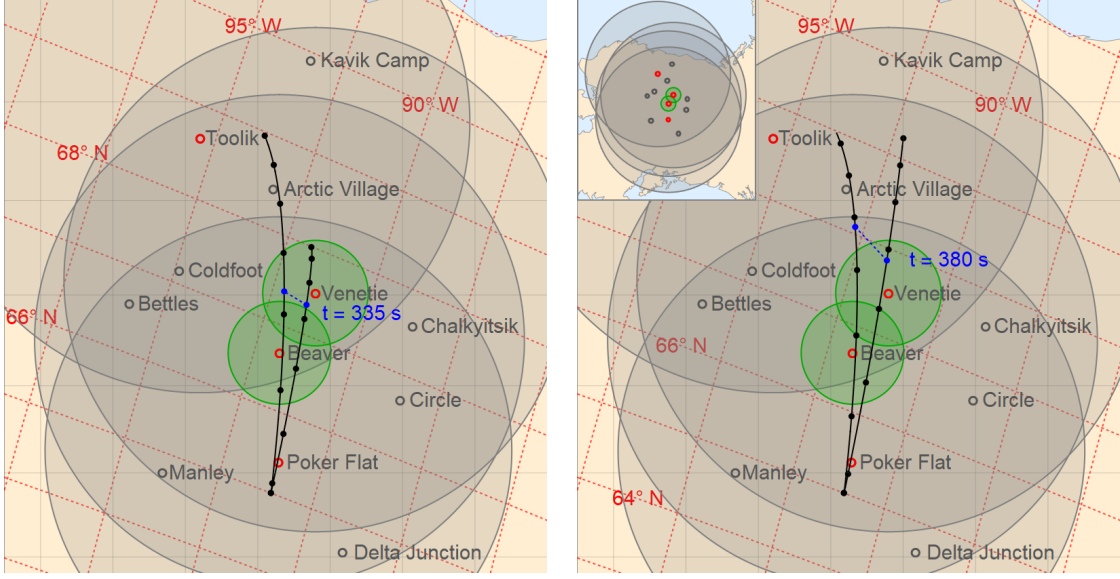


Figure 6: Topdown views of GBO FOVs, footpointed trajectories with relative timing, and lattice sites. (left) The nominal choice of 367 and 430 km altitudes; (right) two 430 km altitude trajectories. Black dots along the trajectories indicate 100 s intervals of flight time, and the blue bar shows MLAT alignment near apogee. Red dashed lines show Apex (magnetic) coordinates. GBO field-of-views are 60° (green), 140° (grey), and 160° (inset).

We note that in the altitude region between 250 km and 800 km, the significant differences in the in situ fields observations will be driven by their azimuthal separation rather than by their altitudes. Thus we can mitigate separation times with different altitudes, since simultaneity in arc crossing time is more important than altitude within this range.

The two main payloads will thus be \sim 50 km separated in the along-arc direction near apogee. For small-scale (few km) separations, the deployed Bob and Rob payloads will provide proxy measurements of local variations as described below and illustrated in Fig. 7.

2.1.2 Traceability matrix

The mission design is tabulated in Figure 8, the Traceability Matrix. We discuss next the various components of the heterogeneous instrumentation and platform arrays: the filtered imagery **GBOs and PFISR** on the ground; the **fields and thermal plasma instruments** on the multipayload in situ platforms; and the **lattice for tomography** connecting them; all tied together using the **GEMINI model** which assimilates and interprets the case study dataset.

2.2 Instruments, groundbased

2.2.1 GBOs

The timing, location, and intensity of optical auroral emissions will be captured by **four dedicated ground-based observatories (GBOs)** covering the two rocket trajectories as illustrated in Fig. 6. We have found (see *Grubbs et al. [2018a, b]; Mella et al. [2011]*)

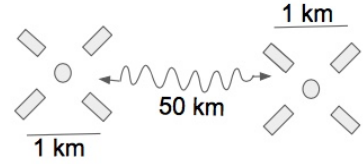


Figure 7: Payload array illustration, showing the relative spacing of the two main payloads, and their clusters of four deployables each. Compare to main-payload separations shown in Fig. 6.

A. Science Goal(s)	B. Science Questions	C. Investigation Objective Requirements			Mission Top Level Requirements
		Measurement	Requirement	Projected Performance	
What mesoscale latitudinal and, particularly, longitudinal, variations exist in plasma flows (electric fields) and volumetric currents at scales of 1-50 km within a non-sheathlike auroral structure's flow-current - conductivity system?	What implications do these non-idealized flow-current - conductivity patterns have for the auroral ionospheric system science (current continuity and energetics) of ionosphere-magnetosphere coupling?	Electric field	2D DC-JULF E-field	range accuracy resolution	up to 100 mV/m (2 km/s) ~ 2 mV/m (50 m/s) 16-bit
		Potential		sampling rate range resolution sampling rate	up to 2 kHz up to +/- 13 V 16-bit ~ 100 samp/s
		Magnetic field	3D DC-JULF B-fields	range resolution sample rate	+/- 80 uT 16 bit ~ 100 samp/s
		Thermal electron temperature	Distribution function slope (ERPA)	sample rate resolution	few Hz <1000K to >4000K 100K
		Plasma density	Current to anode (ERAU-PIP)	sample rate range	10 Hz 1e10 - 5e11 m^-3
		Thermal ion distribution moments (temperature, flow, spacecraft potential)	I-V curve fit parameter (main-PIPs)	sample rate range resolution	10 Hz 0.5 V sweep 25 steps
		Multipoint thermal ion proxies	I-V curve fit parameter (Bob-PIPs)	sample rate range resolution	10 Hz 0.5 V sweep 25 steps
		Electron density maps via tomography lattice	Faraday rotation	resolution net error	less than 6 deg 0.5 TEC
		GBO Auroral emissions to produce maps of electron precipitation parameters	427.8 nm	field of view	better than 0.5 TEC
		EMCCD	557.7 nm	resolution at 110 km frame rate sensitivity	180 deg 0.5 Km 4 Hz
Heliohydrodynamics Goals applicable to GNEISS. "Advance our understanding of ... the connections between solar variability and Earth ..."	and Develop the knowledge and capability to detect and predict extreme conditions...".	scCMOS	844.6 nm	field of view resolution at 110 km frame rate sensitivity	160 deg 0.5 Km 4 Hz 350 rayleighs
		EMCCD (VEE, BEA)		frame rate sensitivity	0.5 Km 4 Hz 2700 rayleighs
		scCMOS (PKR, TOO)	Radar returns	frame rate sensitivity range error	0.5 Km 4 Hz 0.5 Km 400 rayleighs 1000 rayleighs 50-30000 m/s <= 30%
		PFISR plasma flow		cadence	0.5 deg MLAT 3 min
PFISR density				range error	30 sec - 1 min 1e10 - 1e12 m^-3 <= 30%
				spatial resolution cadence	50 - 100 km 3 min

Figure 8: Science Traceability Matrix

Camera	Pixel Size [μm]	Format (h x v)	Pixel FOV [deg]	Min Required Full FOV [deg]	Full FOV [deg]	Max 110 km pixel scale at 40° from center [km]	110 km pixel scale at 40° from center [km]	Required min. sensitivity @ 4 FPS [R]	Projected sensitivity @ 4 FPS [R]	Site	Location	λ (nm)	Type
BLC (EMCCD)	13.0	1024 x 1024	0.17	140.0	180	1.0	0.5	820	300	TOO	Lat/Lon	844.6	sCMOS
											68.63	427.8	EMCCD
											-149.6	557.7	sCMOS
GLC (sCMOS)	13.0	1024 x 1024	0.15	140.0	160	1.0	0.4	2700	600	VEE	Lat/Lon	844.6	EMCCD
											67.01	427.8	sCMOS
											-146.4	557.7	sCMOS
8LC (EMCCD)	13.0	1024 x 1024	0.17	140.0	180	1.0	0.5	550	400	BEA	Lat/Lon	844.6	EMCCD
											66.36	427.8	sCMOS
											-147.4	557.7	sCMOS
8LC (sCMOS)	13.0	1024 x 1024	0.15	140.0	160	1.0	0.4	1000	500	PKR	Lat/Lon	844.6	sCMOS
											65.12	427.8	EMCCD
											-147.4	557.7	sCMOS

Figure 9: GBO locations (right) and performance parameters (left). Each site has three cameras split among two camera designs. Performance requirements are shown with yellow headers, while predicted performance is shown with gray headers.

that ground-based optical observation methods can produce good estimates of the auroral electron spectrum and have the advantage of long-term and simultaneous monitoring over a large continuous area, which is necessary for the broader interpretation of the auroral event to be studied.

Deployment Each GBO site contains three cameras; 1) a blue-line camera (BLC) for the 427.8 nm emission of N_2^+ , 2) a near infrared camera (8LC) for the 844.6 nm emission of atomic O and 3) a green-line camera (GLC) for the 557.7 nm emission of atomic O. Our choices for the four GBO sites are Poker Flat (PKR), Beaver (BEA), Venetie (VEE) and Toolik Lake (TOO). Three sites already have dedicated observatories, while the fourth, Beaver, would be a new site to us, and significantly enhance the outcome of the GNEISS mission. To supply three filtered cameras at each site we will use six **heritage** cameras and six new cameras. The EMCCD-based cameras already in use at Poker Flat were used in the *Grubbs et al.* [2018a, b] analysis of the GREECE and Isinglass rocket missions. Six new cameras were designed and tested on the recent ARCS MIDEX concept study [*Lynch and ARCS Team, 2021*], and use lower cost, high sensitivity sCMOS detectors and COTS optical components for similar sensitivity performance. The sites and the distribution of these imagers are listed in Fig. 9 (right), and shown in Fig. 6.

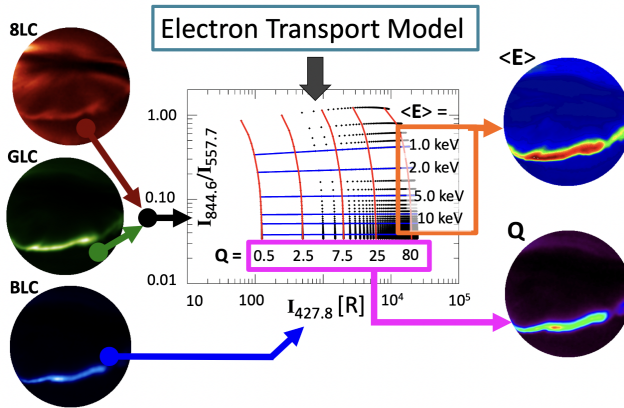


Figure 10: GBO inversion method for VEE and BEA. See *Methodology* text for description.

sitions and create a table of near-IR to green ratio ($I_{844.6}/I_{557.7}$) and blue line intensity ($I_{427.8}$)

Methodology We will use two methods for determining the energy content of the precipitating electrons. The primary method for BEA and VEE, which view the aurora near magnetic zenith, uses calibrated intensities and ratios of three emission lines. The energy flux (Q , mW/m^2) is proportional to the blue (427.8 nm) emission, while the average energy ($\langle E \rangle$, keV) is related to the ratio of the 844.6 nm to 557.7 nm emissions. Figure 10 shows the method for reproducing these two parameters. We use the GLOW model (*Solomon [2001]*) to calculate the emission rates of the three emis-

emission for a range of average energies and energy fluxes of a gaussian electron distribution. When the calibrated images are analyzed, we use this table of intensities and ratios to then read off the predicted energy parameters for each region (down to a single pixel) in the images. These are combined to make maps of the energy flux and average energy.

The views from TOO and PKR are at a large oblique angle which renders the ratio calculation incorrect due to the geometry of the arcs. Therefore, we will employ a method used for Cascades2 (see *Mella et al.* [2011], Fig. 11 therein) of comparing the vertical intensity profile of the GLOW (or similar) model to the measured profiles of the arcs to determine the average energy of the electrons.

Each camera will have a wide field of view $> 160^\circ$, shown in Fig. 6. A smaller field, over which the ratio method will work for VEE and BEA are shown as the smaller circles in the figure. The imaging rate is 4 frames per second (Hz), which will sample the horizontal rocket trajectory at sub-km resolution, and enable detection of along-arc structure motion in the few km/s range. Fig. 9 (left) shows the required and expected sensitivities as well as resolutions of each camera. Once the full resolution images are spatially and intensity calibrated, these level 1 data are inverted to produce a sequence of 2D maps of energy flux (Q , mW/m²) and average energy ($\langle E \rangle$, keV) of an equivalent gaussian electron distribution; these maps are used to drive GEMINI.

2.2.2 PFISR

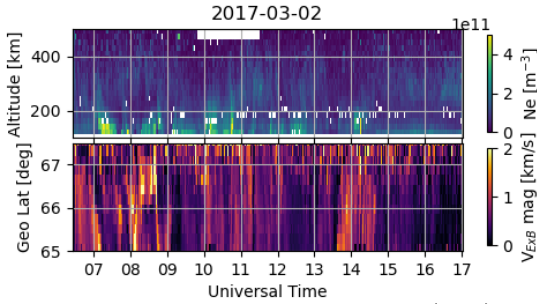


Figure 11: Electron density (top), and plasma drift magnitude (bottom) from processed PFISR data before, during, and after the ISINGLASS rocket launch.

rounding dynamics. GNEISS will use an observation mode with **heritage** from the ISINGLASS sounding rocket in 2017 [*Clayton et al.*, 2019, 2021]. Data will be processed using standard incoherent scatter radar fitting technique at time resolution of 1 minute or less. PFISR also has a real time display which has been used to help evaluate ionospheric conditions for previous Poker Flat launches. PFISR measurements from the ISINGLASS experiment are shown in Figure 11. PFISR provides high-fidelity electron density measurements which will be aggregated with density estimates from the TEC lattice to constrain GEMINI’s initial conditions and validate simulation output.

2.3 Instruments, in situ

Within the context of the groundbased observations, we fly the 2 GNEISS payloads including their 8 deployed Bob and Rob subpayloads. Collectively, these platforms provide **multipoint** observations of **DC electric and magnetic fields E and B**, of **plasma density n_i** , of **thermal electron temperature T_e** , **thermal ion temperature T_i** and **ion drifts v_i** .

2.3.1 Fields: DCE and Mag

Each of the 2 main payloads carries electric and magnetic fields instrumentation. The **Electric Fields Instrument (EFI)** consists of a Quad Stacer Boom (QSB) and a Fields Electronics Box (FEB), which also supports the body-mounted UCB DC-ULF magnetometer (MAG). Figure 12(bottom) illustrates the Quad Stacer Boom (QSB, sans spheres). The electric field sensors are 8-cm diameter graphite-coated (DAG-213) Al spheres deployed in the spin plane on 3-m stroke stacer booms. The spin plane stacer booms and sensors provide a standard two-axis double-probe E field estimate. This QSB allows a single point release of all four stacer booms at a controlled uniform rate for a well-balanced deploy and quiet vehicle dynamics. The **UCB DC-ULF magnetometer (MAG)** is a body-mounted commercial Billingsley TFM65-VQS fluxgate magnetometer.

Power and signal processing for the E-field measurements is provided by the **Fields Electronics Box (FEB)**. The FEB (UCB) provides analog and digital signal processing for a 2D DC-ULF measurement of spin plane E (up to 1 V/m (adjustable) at \sim 1 mV/m accuracy), and 3D B-fields over the \pm 100 μ T range, individual sensor potentials (up to \pm 13 V) at 16-bit resolution and sampling rates up to 2 kHz (1 kHz Nyquist), as well as instrument housekeeping via a serial digital interface to the NSROC TM section.

The UCB Fields package has a long and successful heritage: The QSB has flown dozens of times in the 1980's and 90's on UCB sounding rockets, and more recently on the GREECE, TRICE-2, and ACES2 sounding rocket payloads (36.287 UE Samara, Mar 2014; 52.003/004 Kletzing, Dec 2018). The DC-ULF EFI and MAG electronics flew most recently on the GREECE, TRICE-2, VIPER, INCAA, and ACES2 sounding rockets.

Data temporal and spatial scales Measuring \mathbf{E}_\perp and \mathbf{B} at up to Alfvénic time scales ($<$ 10 Hz) and finer than inertial spatial scales (100 m) resolves the relevant time and length scales for the mesoscale auroral fields physics that GNEISS will probe. Such resolution is achieved via 2 ksamp/s (1 kHz Nyquist) sampling and few km/s payload motion through plasma.

Figure 12 shows data from the two TRICE-2 payloads in the dayside cusp, covering different morphology than the nightside GNEISS, but demonstrating the detailed differences in the spatial distribution of the DC \mathbf{E} and \mathbf{B} fields over the 120-s delay between the two TRICE payloads' traversal of the region. Here the two DCE signatures are shown mapped to their 110-km footprint in geographic latitude and longitude; the two trajectories flew within two minutes of each other.

Deconvolution to data products In order to use the DCE and MAG data to drive GEMINI,

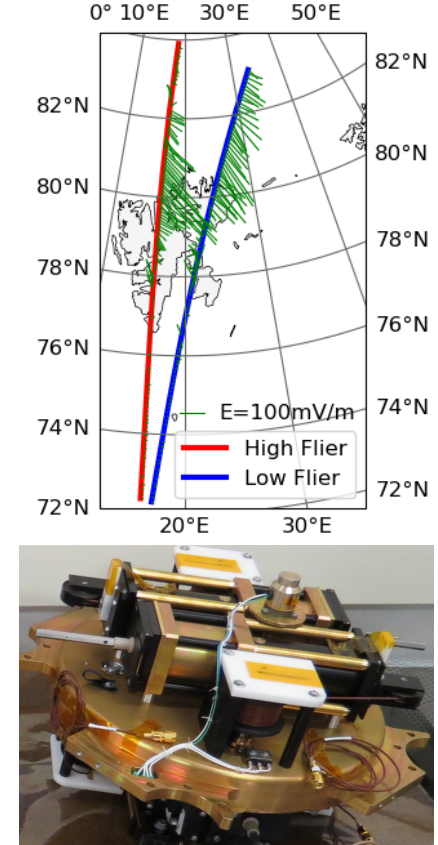


Figure 12: (top) Example DCE data, and (bottom) the stacer boom package. DCE data are shown from a previous mission (TRICE-2), from two nearly-adjacent trajectories.

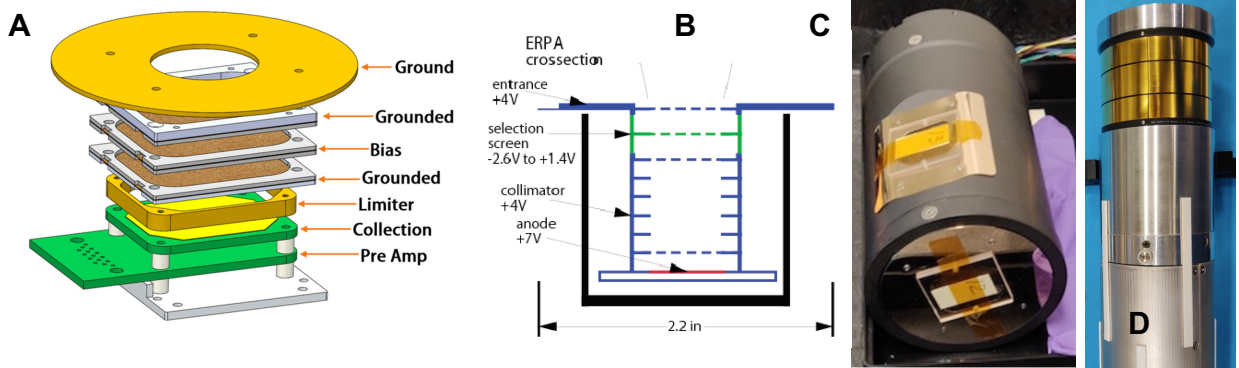


Figure 13: (A) PIP sensor, (B) ERPA sensor, (C) Bob and (D) Rob small deployables.

they must be transformed from the payload coordinate system using the attitude solution and knowledge of the geomagnetic field. The electric field perpendicular to \mathbf{B} is moved to the desired plasma frame and coordinate system via despin and $\mathbf{V} \times \mathbf{B}$ removal, using an $\mathbf{E} \cdot \mathbf{B} = 0$ constraint. In the plasma frame, then, we have the perpendicular \mathbf{E} vector and the deviation of \mathbf{B} from IGRF, along the two main payload trajectories.

As with Isinglass, these data will be combined with information from the imagery defining the along-arc visible arc boundary(ies). We use methodologies derived for the ARCS MIDEX CSR [*Lynch and ARCS Team, 2021*] to find the 2D flow and FAC maps that are most consistent with minimal variation along the arc consistent with the given fields observations (here, along the two trajectories). Interpolation between the trajectories along the curving visible arc boundary, combined with GBO information about the evolving arc boundary and Maxwell's equations, allows us to find the most-likely 2D map of electrostatic potential and FAC consistent with the observations. This is a combination of the single-trajectory version used in [*Clayton et al., 2019, 2021*], with the basis function algorithm derived for ARCS [*Lynch and ARCS Team, 2019*]. These fields maps will be used as drivers for GEMINI runs.

2.3.2 Thermal plasma: PIPs, ERPAs, Bobs, and Robs

GNEISS measures ambient plasma density on the 4 Rob subpayloads; thermal ion temperature and drift on the 2 main payloads and on the 4 Bob subpayloads; and thermal electron temperature on the 2 main payloads. These measurements and platforms are illustrated in Fig. 7 and Fig. 13.

Bobs and PIPs

PIPs The GNEISS main payloads will each carry a suite of eight Petite Ion Probes (PIPs), along with 2 small telemetered “Bob” payloads each carrying two PIPs. The PIPs provide measurements of thermal ion bulk moments. The PIP sensor, developed and tested in Dartmouth’s thermal laboratory plasma experiment [*Frederick-Frost and Lynch, 2007; Fisher et al., 2016; Roberts et al., 2017a*], is a small collimated retarding potential analyzer (RPA) used in a subsonic regime inside the (negatively charged) payload sheath [*Siddiqui et al., 2011*]. The PIP has flown on a number of recent sounding rockets, and its operation and analysis are detailed in *Fraunberger et al. [2020]*, and earlier in [*Fisher et al., 2016; Roberts et al., 2017a*]. Results are constrained using available information from other sensors such as electron temperature from the ERPA, payload motion from the GPS, and flow velocity from the DCE. An updated version of this approach is in work for analysis of the recent Kinet-X,

Crex-2, and Lamp PIP data. Newer PIPs are higher-gain, and better mounted, improving on the predicted capabilities.

Bobs The Bob payloads themselves (see Fig. 13) are small subpayloads ejected in a plane perpendicular to the main payload spin axis (and thus to the magnetic field). These “Bob” subpayloads were originally designed and flown for the Isinglass flight (Poker 2017), with a preliminary test flight from Wallops (Hesh 2015). Each Bob carries two PIPs, an Arduino-based spacecraft bus, and a commercial inertial measurement unit (IMU) for evaluating Bob attitude and separation vector, information needed for PIP analysis. The NSROC-provided Dallas bus section provides power and telemetry. A full description of the Isinglass/Hesh Bob payloads can be found in *Roberts et al.* [2017a, b]. Figure 13 shows an image of the Bobs as used for Delamere/Kinet-X.

The PIPs have extensive and ongoing **heritage** of use on recent sounding rocket payloads including LAMP, Kinet-X, CREX-2, and Isinglass. The Bob payloads, developed in parallel with the NSROC Dallas subsystem, are an ongoing but stable development design. Their most recent use is the ongoing Apophis mission, in parallel with the ERAU “Rob” payload described below.

PIP data GNEISS will use PIP data to estimate plasma parameters in two different ways. On the main payload, an array of PIPs in a plane tangential to the payload deck, with various elevation angles (similar to Isinglass,) will be analyzed as in *Fraunberger et al.* [2020] to find thermal ion temperatures and payload potential levels. These main payload PIP data can then be compared to proxy observations from the Bob-mounted PIPs on the small deployables.

Secondly, on the Bob subpayloads, the PIP data will be used with a different emphasis. Here the focus will be on looking for small-scale variations in the plasma parameters as compared to the main payload observations. Figure 14(top), from Isinglass illustrates early analysis of the differing plasma signature proxies seen by two Bob PIPs looking in the N-W direction but separated by approximately one km. The signature delays seen by the different Bobs as they exit an Alfvénic region are shown between T+250 and T+251 s.

n_i and *Rob*s

ERAU PIPs The ERAU Positive Ion Probe (ERAU-PIP) is a Langmuir probe instrument

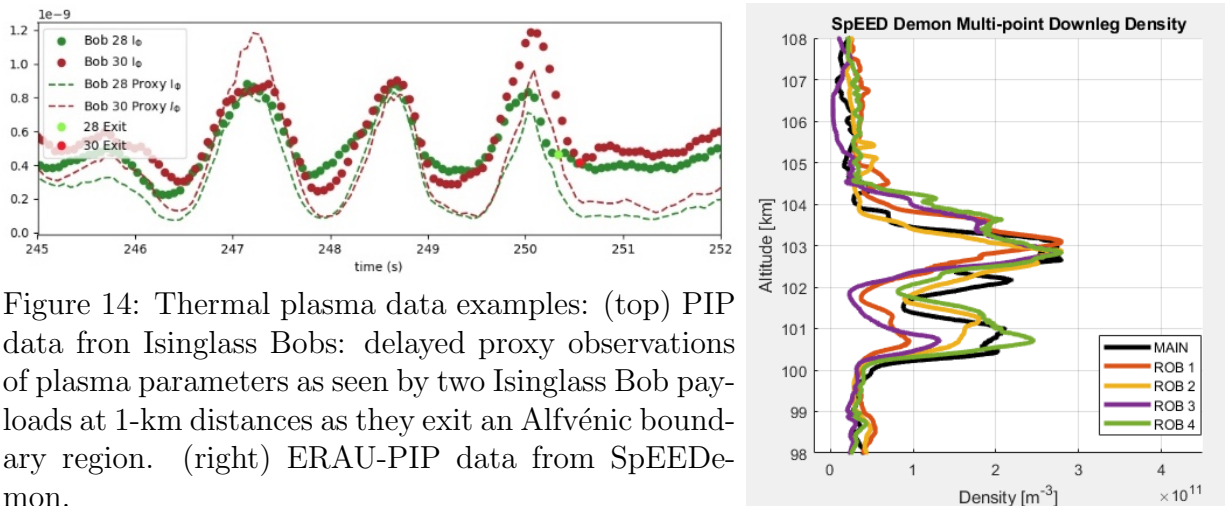


Figure 14: Thermal plasma data examples: (top) PIP data from Isinglass Bobs: delayed proxy observations of plasma parameters as seen by two Isinglass Bob payloads at 1-km distances as they exit an Alfvénic boundary region. (right) ERAU-PIP data from SpEEDemon.

on a Rob subpayload which maintains a fixed-bias in the ion saturation region. The probe is biased negative with respect to the plasma so that electrons are repelled, and positive charge is collected on the instrument's conductive surface. Analysis of the collected current allows for high-cadence in-situ measurements of relative change in ion density; since the collecting anode cylindrically wraps the Rob, the data are relatively insensitive to payload attitude, unlike the collimated PIPs. Figure 14(right) shows recent calibrated current measurements acquired by Rob subpayloads and main payload ERAU-PIP instruments (from SpEED Demon). The sensitivity of each proved sufficient to clearly resolve the E layer and several instances of small high-frequency fluctuations in ion density.

Rob The Rob subpayloads (see Fig. 13 also contain an accelerometer and magnetometer measurement, to provide orientation and low altitude drag information. This **heritage** instrument and subpayload design has been flown on the SpEED Demon mission, and will be flown on the upcoming Apophis and SEED missions.

T_e and ERPA

ERPA Figure 13 illustrates the small ERPA sensor. Design and operation of the high-heritage ERPA is well-described in the literature [Cohen *et al.*, 2016; Frederick-Frost and Lynch, 2007]. The ERPA covers an energy range of about 0 to 3 eV with steps of 0.06 eV. The primary data product of the ERPA is electron temperature T_e , obtained by fitting an exponential to the high energy tail of the thermal electron distribution function. The temperature measurement depends only on the slope parameter so temperature can be derived without knowing density or payload potential.

ERPA heritage is extensive, with flights on many sounding rockets including Isinglass, Delamere-Kinet-X, and CREX-2. Observations from previous rocket missions span environments up to over 4000K (Sciifer-2, [Frederick-Frost and Lynch, 2007]) and below 1000K (ACES-HIgh, [Cohen *et al.*, 2013]).

ERPA data T_e is provided at 8 Hz cadence on each of the two main payloads, which are separated by approximately 50 km. Error estimates for the temperature data product have a mean error of less than 5 percent in the temperature determination. This tight constraint on T_e greatly complements the PIP thermal ion analysis, as it provides a strong estimate for the payload potential, which varies strongly with auroral precipitation (see Fraunberger *et al.* [2020]). The electron temperature is a sensitive proxy for many aspects of the auroral environment, showing strong, prompt, and direct responses to auroral precipitation.

2.4 Instruments, lattice

Finally, between the in situ and the GBO observations, we have the **lattice**. The GNEISS **lattice** design explicitly explores the low-resource end of this family of experiments: providing useful distributed plasma density profiles in the volume of space between the GNEISS in situ observations and the GBOs.

2.4.1 Lattice Definition and Justification

The GNEISS **lattice** system offers a remote sensing tool to estimate 2D slices of electron density by measuring the **Faraday rotation** of radio signals and hence ionosphere total electron content (TEC) along lines of sight between the rocket-borne transmitters and ground-based receivers. The **lattice** introduces an RF active experiment in which the (NSROC-provided)

RF signals at very high frequencies (VHF) (~ 150 MHz) are broadcast from each of the 2 GNEISS main payloads, and received at 12 (experimenter-provided) receivers distributed in the vicinity of rocket trajectories (4 beneath the trajectories, 4 to the east and 4 to the west of trajectories), as illustrated in Figures 5 and 6. Figure 15 shows another view of the planned observational geometry. Note that GNEISS lattice Faraday rotation experiment is different from the dual-frequency GPS/beacon technique that relies on differential phase from two phase-coherent signals [e.g. *Heise et al.*, 2002; *Bernhardt et al.*, 2006].

The GNEISS **lattice** implementation offers several advantages compared to conventional GPS TEC imaging: (a) It estimates the TEC between rocket altitudes and the ground, whereas the GPS TEC data includes contributions from the plasmasphere and the topside ionosphere. (b) It estimates TEC directly directly below the rockets (elevation angles close to 90 deg). The inclination of GPS satellites does not allow for high elevation angle TEC measurements at Poker Flat latitudes. (c) Signals with lower frequency (e.g. VHF) are affected much more by the ionosphere and provide more accurate measurements (higher rotation angle or differential phase) than GPS TEC in this region.

The transmitted signals from the two rockets are requested to be continuous wave (CW) linearly polarized and slightly off (~ 10 kHz) from each other in frequency to enable transmitter identification (see Hardware section below). The groundbased receivers will be based on a software-defined radio (SDR) platform, and equipped with cross-dipole antennas to allow for measuring the polarization of the received signals.

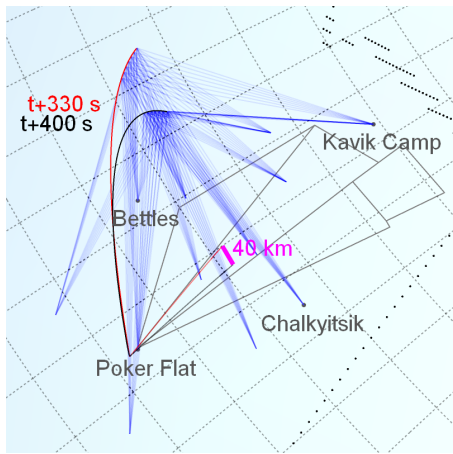


Figure 15: Lattice observational geometry. A subset of lattice lines of sight is shown in blue.

dependent on the angle between \mathbf{B} and the line of sight.

2.4.2 Hardware

The lattice hardware consists of VHF transmitters on the main payloads, and software-defined radio (SDR) receiver stations spread below the trajectories.

Lattice transmitter needs: Each of the two GNEISS main payloads is requested to carry a NSROC-provided VHF transmitter; the two transmitters shall be at slightly different frequencies (~ 10 kHz) so that they can be distinguished by the narrow-band receivers. They are to be linearly polarized, at 1-5 W transmission power of continuous carrier wave. We are requesting that NSROC supply these transmitters. Commercial (ie, comparable to cubesat

hardware but at VHF frequencies) transmitters suggested by Prof James LaBelle's design engineer at Dartmouth, Mr David McGaw, include these from bigredbee [Bigredbee, 2023], from QRP labs [QRP, 2023], or from radiometrix [Radiometrix, 2023]. For the linear-polarization transmission antenna, Mr McGaw suggests two half-m pop-out rods deployed radially outward, perpendicular to the (field-aligned) spin axis. As noted at the beginning and end of this lattice section, the lattice experiment is exploring the low-resource end of a range of similar experiments, and we encourage NSROC to find a simple low-resource solution that meets the requirements: \sim 150MHz and \sim 150.010MHz, 1-5W, linear polarized CW transmissions. The direction of the linear polarization does not matter (it will spin with the payload), other than that it be roughly horizontal (perpendicular to the field-aligned spin axis.) We note that several other research groups are exploring similar goals, and there may well be overlap that can be exploited as noted in the Heritage discussion below.

Lattice receiver array hardware: The array of lattice receivers, pictured in the mission diagrams above, will be developed and operated by the Dartmouth student group of Professor Lynch's 317 Lab, benefiting from mentoring by the adjacent highly experienced RF experimental group led by Professor LaBelle. The UAF/GI team will be responsible for the physical placement of the receivers at the Alaskan field sites, many of which are native villages. Dartmouth will donate the Starlink portals to the villages after the mission is complete. Each lattice receiver station, as illustrated in Figure 16, consists of a residential-class Starlink station [Starlink, 2023], an RSPduo software-defined radio from SDRplay [SDRplay, 2023], a small NUC computer [NUC, 2023], GPS timestamping of the received data, and a 1-m crossed-dipole antenna with an associated dual preamplifier. The only requirement at the field site is line power, and snow clearance. The predicted purchase and fabrication costs are \$1600 per site, half of which is the Starlink hardware and usage costs.

Lattice receiver design specifications: As illustrated in the next section on lattice analysis, the expected Faraday rotation of the polarization of the transmissions ranges up to to 180° for the Isinglass-scenario example shown (this is in addition to the rotation with payload spin, which will be known from the attitude solution and the GPS timestamping at the receiver sites.) As we demonstrate below, our low-resource lattice system provides useful density reconstruction profiles when each line of sight can measure TEC \pm 0.5 TECU; from Eqn. (2) at 150 MHz, this corresponds to an angular uncertainty of better than 10 deg. Note that for a line of sight parallel to \mathbf{B} of 1 TECU, the rotation angle is $\sim 30^\circ$.

The uncertainty in the received angle of polarization depends on the uncertainty in the individual cross dipole antenna voltages, which in turn depend on the signal-to-noise of the link between transmitter and receiver. We used a standard link margin calculator [i.e., Friis Transmission Equation Calculator, [Friis, 2023]] and the following link parameters to determine a receiver signal-to-noise ratio of no less than 35 dB. For a 1 W, EIRP of 2.1 dBW

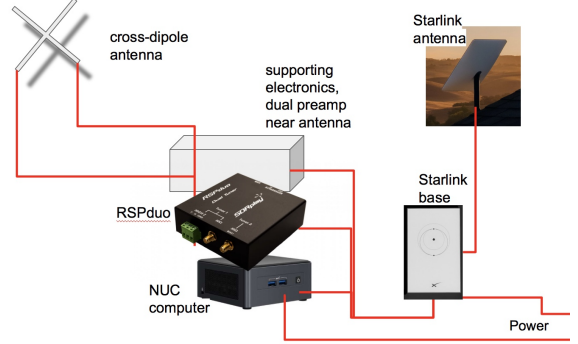


Figure 16: Block diagram of lattice receiver station; 12 of these will be fielded in the Alaska regions of the GNEISS trajectories [NUC, 2023; Starlink, 2023; SDRplay, 2023].

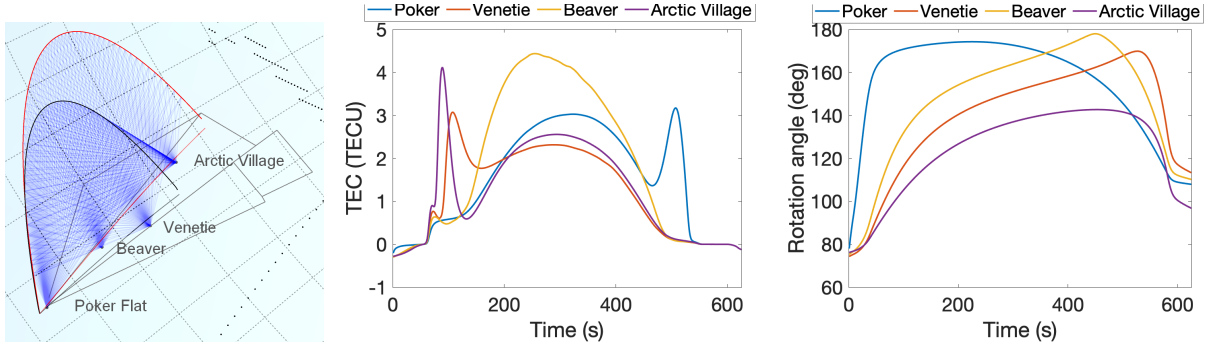


Figure 17: (a) Lines of sight between the rockets and four receivers (Poker, Venetie, Beaver, Arctic Village). (b) Time series of expected TEC between rocket 1 and the four receivers). (c) Time series of expected rotation angle between rocket 1 and receivers.

transmission, and assuming transmitter-receiver angular misalignment of 45° , and a slant distance of 500 km, the received signal strength is calculated to be -131.76 dBW. Using a pre-amplifier on the received antenna with a noise figure of 0.5 dB, the receiver thermal noise (which dominates the noise at these frequencies, over other factors such as sky noise) is -173 dBW. Thus the carrier-to-noise ratio (CNR) is 41 dB at 500 km distance, and 35 dB at 1000 km distance. Thus for any line of sight the signal-to-noise shall be better than 20 dB, corresponding to a 10% uncertainty of the measured voltage on either antenna. That uncertainty leads to an uncertainty of 14% in the total amplitude of the signal, and a 0.1 radian (5.8°) uncertainty in the polarization of the signal, at least a factor of 1.5 more accurate than that required to achieve the GNEISS TEC measurements.

Heritage (or lack thereof): The GNEISS **lattice** experiment is a new design based on well-established principles and existing commercial hardware. Several other experimental groups are pursuing similar goals, given the importance of distributed ionospheric density data to our community’s system science goals. Higher fidelity experiments include the beacon experiment (Dr P. Bernhardt) flying on the GIRAFF mission (PI R. Michell, GSFC), and the longstanding Friedrich HF experiment [Friedrich, 2016]). Another new development from Clemson University involves the provision of a technology demonstration payload, as part of a proposed (LAMP-2, A. Jaynes, PI) mission, building on the Seddon [1953] and Friedrich [2016] designs. The GNEISS **lattice** is explicitly designed to explore the low-resource end of this regime, which has the potential to become quite valuable to our community. The science information from the lattice for the GNEISS mission is backed up by the overlapping information from the GBOs, and from PFISR, for science closure.

2.4.3 Analysis: TEC sensitivity and reconstruction

From the measured RF rotation angles for each ray path, we compute the TEC for each ray path using Eqn. (2), and from the linear relationship between TEC and the underlying electron density, $TEC = \int n_e dl$, we estimate (reconstruct) 2D density structures in three different planes (two slant planes as shown in Fig. 5, plus one vertical plane below the rocket trajectories.) These three different planes will show the longitudinal variability in density.

For density reconstructions, we use linear tomographic techniques [e.g. Bernhardt *et al.*, 1998; Karl, 2005] to invert this linear system of equations. Because ionosphere tomography is a limited angle tomography, we leverage constrained tomography procedure to impose *a priori* information (such as smoothness constraints or parametric modeling) and stabilize

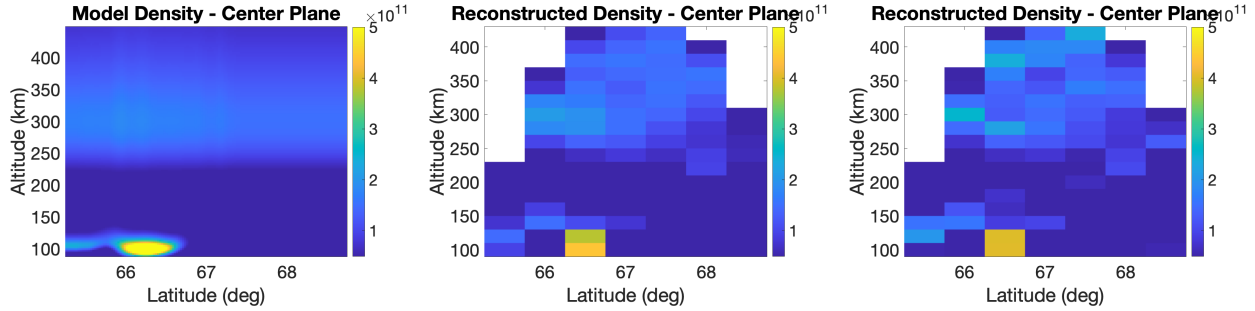


Figure 18: (a) Modeled 2D density. (b) reconstructed density using TEC error of 0.1 TECU. (c) reconstructed density using TEC error of 0.5 TECU (digitized TEC).

the solution in the presence of noise [e.g. *Austen et al.*, 1988; *Nikoukar et al.*, 2008, 2015].

To illustrate and assess the performance of reconstruction, we “fly” the rockets and create a simulated lattice through a simulated auroral ionosphere. Focusing on the center plane (lines of sight in Fig. 17(a)), we compute the TEC along the trajectory with 1-s cadence (b) and the expected Faraday rotation angle using IGRF B field (c). For density inversion, we convert the expected measurement angles (noise added) to TEC estimates using Eqn. (2) for the center plane. Next, we discretize the 2D plane below the rockets as a function of altitude (20 km spacing) and latitude (0.3° spacing) while assuming constant longitude. We then compute the forward model for the observation geometry (the matrix relating TEC to density) based on the length of each ray passing through each pixel of the grid. The final step is the linear inversion of the matrix equation to determine the density structure, which in turn amounts to optimization of a constrained cost function. Edge-preserving constraints, such as Total Variation [e.g. *Vogel*, 2002] are applied to allow for detection of sharp density enhancements due to auroral precipitation, while stabilizing solution in the presence of noise. The fusion of data from other instruments (e.g., PFISR, in situ density [e.g. *Aa et al.*, 2022]) will be included in form of additional constraints during the development phase. Figure 18(a) shows the modeled 2D structures used for this analysis, while Figure 18(b) illustrates the reconstructed 2D density for the center plane. Figure 18(c) shows reconstruction when we digitize the TEC to nearest integer values (maximum ± 0.5 TECU error). This shows that the available lines of sight and RF system design provide for the robust reconstruction of the E and F region densities required by GNEISS. As with PFISR data, the lattice data will be used by to constrain GEMINI’s initial conditions and validate simulation output.

2.5 Modelling tools

The Geospace Environment Model of Ion-Neutral Interactions (GEMINI) is a 3D, local-scale, multifluid-electrodynamic model of the ionosphere [GEMINI, 2023]. The mathematical formulation of GEMINI comprises a fluid system of equations (conservation of mass, momentum, and energy) which is coupled to a current continuity equation. GEMINI can accommodate flexible meshes (E-region through topside altitudes) and is configurable to accept user-defined, arbitrary boundary and initial conditions, including field-aligned currents (or convection electric fields) and suprathermal electron precipitation. From these inputs the model computes electric fields, currents, magnetic fields, and plasma parameters (density, temperature, and drift) throughout the full simulation volume. The input flexibility, ability to resolve sub-km dynamics, and self-consistent treatments of ionospheric electrodynamics makes GEMINI a good choice for application to the GNEISS datasets. GEMINI’s heritage

has been established in a number of our prior studies [Zettergren and Semeter, 2012; Zettergren et al., 2014, 2015; Lamarche et al., 2022], and use of the model in the GNEISS mission will build off of data-driven capabilities from Clayton et al. [2021].

3 Science Closure, Relevance, and Impact

Closure: from measurement to science While there is much that we understand about discrete nightside aurora, there is still so very much to learn – GNEISS measurements address specifically the unobserved in situ nature of along-arc variations in the auroral system and provides specifications for unknown aspects of auroral inputs (science question 1, Sec. 1.2.3).

Our second science question invites some specific implementations. As just one example, by combining the detailed in situ and remote sensing observations of the auroral drivers and ionospheric response using GEMINI modeling, GNEISS will enable a clearer understanding of how along-arc structure affects the coupling of the arc to its ionospheric environment such as background fields from convection.

Relevance and impact for Heliophysics As noted at the end of Section 1.1, GNEISS has many points of NASA relevance. We note further here that the GNEISS exploration of auroral ionosphere mesoscales is a system science study; successful implementation and a path to closure require the synthesis of our heterogeneous datasets through physics-based models. This methodology is directly in line with the Heliophysics Decadal Survey DRIVE recommendations: “...system science requires new types of configurations of observations...” used in “computational models that extract essential physics from measurements made across multiple observing platforms” [NRC, 2013]; as well as with Key Science Goals (KSGs) 2: “Determine the dynamics and coupling of Earth’s magnetosphere, ionosphere ... requiring research approaches that treat it as a coupled system.” and KSG4: “Discover and characterize fundamental processes that occur ... within the heliosphere....” [NRC, 2013].

4 Management

4.1 Team and Responsibilities:

Our team responsibilities are as follows. *Lynch*, PI, is responsible for the GNEISS effort overall and the PIPs, Bobs, and lattice receivers specifically. *Bonnell*, DCE and MAG. *Burleigh*, GEMINI modelling. *Clayton*, ERAU-PIPs and Robs. *Hampton*, GBOs. *Lamarche*, PFISR. *Lessard*, ERPAs. *Nikoukar*, lattice inversion analysis. *Samara*, imagery inversion analysis. *Zettergren*, GEMINI modelling. The entire team will participate in and contribute to science effort and student mentoring.

4.2 Schedule and Work Plan:

Year 1: Sept 2023 - Aug 2024 MIC, project design.

Year 2: Sept 2024- Aug 2025 DR, fabrication, begin integration.

Year 3: Sept 2025 - Aug 2026 complete integration, MRR, PFISR mode design/coordination, launch campaign, analysis.

The scheduled launch campaign is in Feb 2026. The nominal window is Feb 10 - 22, 2026 (new moon on Feb 17th). The secondary window is Mar 12 - 24, 2026 (new moon Mar 19th). Note that the predicted peak of the solar cycle as per SWPC is July of 2025.

Our team looks forward to this opportunity and will bring enthusiasm and commitment to the effort.

GNEISS:

GEOPHYSICAL NON-EQUILIBRIUM IONOSPHERIC SYSTEM SCIENCE
Kristina A Lynch, Dartmouth College, HLCAS-2023

References

- Aa, E., S.-R. Zhang, P. J. Erickson, W. Wang, A. J. Coster, and W. Rideout, 3-D Regional Ionosphere Imaging and SED Reconstruction With a New TEC-Based Ionospheric Data Assimilation System (TIDAS), *Space Weather*, 20(4), doi:10.1029/2022SW003055, 2022.
- Austen, J. R., S. J. Franke, and C. H. Liu, Ionospheric imaging using computerized tomography, *Radio Science*, 23(3), 299–307, doi:10.1029/RS023i003p00299, 1988.
- Bernhardt, P. A., C. L. Siefring, I. J. Galysh, T. F. Rodilosso, D. E. Koch, T. L. MacDonald, M. R. Wilkens, and G. P. Landis, Ionospheric applications of the scintillation and tomography receiver in space (CITRIS) mission when used with the DORIS radio beacon network, *Journal of Geodesy*, 80(8-11), 473–485, doi:10.1007/s00190-006-0064-6, 2006.
- Bernhardt, P. A., et al., Two-dimensional mapping of the plasma density in the upper atmosphere with computerized ionospheric tomography (cit), *Physics of Plasmas*, 5(5), 2010–2021, doi:10.1063/1.872872, 1998.
- Bigredbee, 5 Watt RF transmitter beacon, <https://shop.bigredbee.com/products/2m-5watt-fm-beacon>, [Online; accessed January-2023], 2023.
- Brekke, A., C. Hall, and T. Hansen, Auroral ionospheric conductances during disturbed conditions, in *Annales Geophysicae*, vol. 7, pp. 269–280, 1989.
- Clayton, R., et al., Two-dimensional maps of in situ ionospheric plasma flow data near auroral arcs using auroral imagery, *Journal of Geophysical Research: Space Physics*, 124(4), doi:10.1029/2018JA026440, 2019.
- Clayton, R., et al., Examining the auroral ionosphere in three dimensions using reconstructed 2D maps of auroral data to drive the 3D GEMINI model, *Journal of Geophysical Research: Space Physics*, 126(11), doi:10.1029/2021JA029749, 2021.
- Cohen, I. J., M. Widholm, M. R. Lessard, P. Riley, J. Heavisides, J. I. Moen, L. B. N. Clausen, and T. A. Bekkeng, Rocket-borne measurements of electron temperature and density with the electron retarding potential analyzer instrument, *Journal of Geophysical Research: Space Physics*, doi:10.1002/2016JA022562, 2016.
- Cohen, I. J., et al., Auroral Current and Electrodynamics Structure (ACES) observations of ionospheric feedback in the Alfvén resonator and model responses, *Journal of Geophysical Research (Space Physics)*, 118, 3288–3296, doi:10.1002/jgra.50348, 2013.

Fang, X., C. E. Randall, D. Lummerzheim, S. C. Solomon, M. J. Mills, D. R. Marsh, C. H. Jackman, W. Wang, and G. Lu, Electron impact ionization: A new parameterization for 100 eV to 1 MeV electrons, *Journal of Geophysical Research: Space Physics*, 113(A9), doi:10.1029/2008JA013384, 2008.

Fisher, L., et al., Including sheath effects in the interpretation of planar retarding potential analyzer's low-energy ion data, *Review of Scientific Instruments*, 87(4), 043,504, 2016.

Fraunberger, M., K. A. Lynch, R. Clayton, T. M. Roberts, D. Hysell, M. Lessard, A. Reimer, and R. Varney, Auroral ionospheric plasma flow extraction using subsonic retarding potential analyzers, *Review of Scientific Instruments*, 91, doi:10.1063/1.5144498, 2020.

Frederick-Frost, K., and K. Lynch, Experimental studies of low density and temperature ion and electron sheaths, *Physics of Plasmas*, 14(12), 123,503, 2007.

Friedrich, M., *Handbook of the Lower Ionosphere*, 200 ed., Verlag der Technischen Universität Graz, 2016.

Friis, RF Friis Transmission Calculator Formula, <https://www.pasternack.com/t-calculator-friis.aspx>, [Online; accessed January-2023], 2023.

Fung, S. F., R. F. Benson, I. A. Galkin, J. L. Green, B. W. Reinisch, P. Song, and V. Sonwalkar, Radio-frequency imaging techniques for ionospheric, magnetospheric, and planetary studies, in *Understanding the Space Environment through Global Measurements*, edited by Y. Colado-Vega, D. Gallagher, H. Frey, and S. Wing, pp. 101–216, Elsevier, doi:10.1016/B978-0-12-820630-0.00006-4, 2022.

GEMINI, <https://github.com/gemini3d/gemini3d>, [Online; accessed January-2023], 2023.

Grammarist, <https://grammarist.com>, [Online; accessed January-2023], 2023.

Grubbs, G., R. Michell, M. Samara, D. Hampton, J. Hecht, S. Solomon, and J.-M. Jahn, A comparative study of spectral auroral intensity predictions from multiple electron transport models, *Journal of Geophysical Research: Space Physics*, 123(1), 993–1005, 2018a.

Grubbs, G., R. Michell, M. Samara, D. Hampton, and J.-M. Jahn, Predicting electron population characteristics in 2-D using multispectral ground-based imaging, *Geophysical Research Letters*, 45(1), 15–20, 2018b.

Gurnett, D. A., and A. Bhattacharjee, *Introduction to Plasma Physics*, 2005.

Hallinan, T. J., J. Kimball, H. C. Stenbaek-Nielsen, K. Lynch, R. Arnoldy, J. Bonnell, and P. Kintner, Relation between optical emissions, particles, electric fields, and alfvén waves in a multiple rayed arc, *Journal of Geophysical Research: Space Physics*, 106(A8), doi:10.1029/2000JA000321, 2001.

Heise, S., N. Jakowski, A. Wehrenpfennig, C. Reigber, and H. Lühr, Sounding of the topside ionosphere/plasmasphere based on GPS measurements from CHAMP: Initial results, *Geophysical Research Letters*, 29(14), doi:10.1029/2002GL014738, 2002.

- Karl, C., Regularization in image restoration and reconstruction, in *Handbook of Image and Video Processing*, edited by A. Bovik, pp. 183–202, Academic Press, 2005.
- Klatt, E., P. Kintner, C. Seyler, K. Liu, E. MacDonald, and K. Lynch, SIERRA observations of Alfvénic processes in the topside auroral ionosphere, *Journal of Geophysical Research: Space Physics*, 110(A10), 2005.
- Knight, S., Parallel electric fields, *Planetary and Space Science*, 21(5), 741–750, doi:10.1016/0032-0633(73)90093-7, 1973.
- Lamarche, L., K. Deshpande, and M. Zettergren, Observations and modeling of scintillation in the vicinity of a polar cap patch, *J. Space Weather Space Clim.*, 12(27), doi:10.1051/swsc/2022023, 2022.
- Lynch, K., and ARCS Team, Auroral Reconstruction CubeSwarm – ARCS: A NASA Heliophysics mission concept for decoding the aurora, AGU Fall Meeting, 2019.
- Lynch, K., and ARCS Team, Auroral Reconstruction Cube Sat MIDEX Concept Study Report, delivered to NASA Heliophysics, 2021.
- Lynch, K., et al., MICA sounding rocket observations of conductivity-gradient-generated auroral ionospheric responses: Small-scale structure with large-scale drivers, *Journal of Geophysical Research: Space Physics*, 120(11), doi:10.1002/2014JA020860, 2015.
- Lynch, K. A., et al., Auroral ion outflow: Low altitude energization, *Annales Geophysicae*, 25(9), doi:10.5194/angeo-25-1967-2007, 2007.
- Mallinckrodt, A. J., A numerical simulation of auroral ionospheric electrodynamics, *Journal of Geophysical Research: Space Physics*, 90(A1), 409–417, doi:10.1029/JA090iA01p00409, 1985.
- Marghitu, O., *Auroral Arc Electrodynamics: Review and Outlook*, pp. 143–158, American Geophysical Union (AGU), doi:10.1029/2011GM001189, 2012.
- Mella, M. R., et al., Sounding rocket study of two sequential auroral poleward boundary intensifications, *Journal of Geophysical Research: Space Physics*, 116(A1), doi:10.1029/2011JA016428, 2011.
- National Research Council, Solar and Space Physics: A Science for a Technological Society, Washington, DC: The National Academies Press, doi:10.17226/13060, Decadal Survey, 2013.
- Nicolls, M. J., and C. J. Heinselman, Three-dimensional measurements of traveling ionospheric disturbances with the poker flat incoherent scatter radar, *Geophysical Research Letters*, 34(21), doi:10.1029/2007GL031506, 2007.
- Nikoukar, R., F. Kamalabadi, E. Kudeki, and M. Sulzer, An efficient near-optimal approach to incoherent scatter radar parameter estimation, *Radio Science*, 43(05), 1–15, doi:10.1029/2007RS003724, 2008.

Nikoukar, R., G. Bust, and D. Murr, A novel data assimilation technique for the plasmasphere, *Journal of Geophysical Research: Space Physics*, 120(10), 8470–8485, doi: 10.1002/2015JA021455, 2015.

NUC, Intel nuc, <https://www.intel.com/content/www/us/en/products/details/nuc.html>, [Online; accessed January-2023], 2023.

QRP, QRP Labs - Ultimate3S QRSS/WSPR kit, <http://shop.qrp-labs.com/U3S>, [Online; accessed January-2023], 2023.

Radiometrix, Real radios for real applications product search, <http://www.radiometrix.com/content/hx1>, [Online; accessed January-2023], 2023.

Roberts, T., K. Lynch, R. Clayton, J. Weiss, and D. Hampton, A small spacecraft for multipoint measurement of ionospheric plasma, *Review of Scientific Instruments*, 88(7), 073,507, 2017a.

Roberts, T. M., K. A. Lynch, R. E. Clayton, M. E. Disbrow, and C. J. Hansen, Magnetometer-based attitude determination for deployed spin-stabilized spacecraft, *Journal of Guidance, Control, and Dynamics*, 40(11), 2941–2947, 2017b.

Robinson, R., R. Vondrak, K. Miller, T. Dabbs, and D. Hardy, On calculating ionospheric conductances from the flux and energy of precipitating electrons, *Journal of Geophysical Research: Space Physics*, 92(A3), 2565–2569, 1987.

SDRplay, <https://www.sdrplay.com/docs/RSPduoDatasheetV0.5.pdf>, [Online; accessed January-2023], 2023.

Seddon, J. C., Propagation measurements in the ionosphere with the aid of rockets, *Journal of Geophysical Research (1896-1977)*, 58(3), 323–335, doi:10.1029/JZ058i003p00323, 1953.

Siddiqui, M., L. Gayetsky, M. Mella, K. Lynch, and M. Lessard, A laboratory experiment to examine the effect of auroral beams on spacecraft charging in the ionosphere, *Physics of Plasmas*, 18(9), 092,905, 2011.

Solomon, S., Auroral particle transport using Monte Carlo and hybrid methods, *Journal of Geophysical Research: Space Physics*, 106(A1), doi:10.1029/2000JA002011, 2001.

Starlink, <http://starlink.com>, [Online; accessed January-2023], 2023.

Stix, T. H., *Waves in plasmas*, 1992.

Swarm, <https://earth.esa.int/eogateway/missions/swarm/data>, [Online; accessed January-2023], 2023.

Themis, <https://data-portal.phys.ucalgary.ca/>, [Online; accessed January-2023], 2023.

Vogel, C. R., *Computational Methods for Inverse Problems*, *Frontiers in Applied Mathematics*, vol. 23, SIAM, doi:10.1137/1.9780898717570, 2002.

Zettergren, M., and J. Semeter, Ionospheric plasma transport and loss in auroral downward current regions, *Journal of Geophysical Research: Space Physics*, 117(A6), doi:10.1029/2012JA017637, 2012.

Zettergren, M., J. Semeter, and H. Dahlgren, Dynamics of density cavities generated by frictional heating: Formation, distortion, and instability, *Geophysical Research Letters*, 42(23), doi:10.1002/2015GL066806, 2015.

Zettergren, M., et al., Auroral ionospheric F region density cavity formation and evolution: MICA campaign results, *Journal of Geophysical Research: Space Physics*, 119(4), doi: 10.1002/2013JA019583, 2014.